
Article:
Hack, J. orcid.org/0000-0002-5529-4750, Ziesche, R.F. orcid.org/0000-0001-7955-6893, Fransson, M. et al. (7 more authors) (2024) Understanding water dynamics in operating fuel cells by operando neutron tomography: investigation of different flow field designs. Journal of Physics: Energy, 6 (2). 025021. ISSN 2515-7655

https://doi.org/10.1088/2515-7655/ad3984

Understanding water dynamics in operating fuel cells by operando neutron tomography: investigation of different flow field designs

Journal of Physics: Energy

PAPER

Understanding water dynamics in operating fuel cells by operando neutron tomography: investigation of different flow field designs

Jennifer Hack[1,2,3,*], **Ralf F Ziesche**[4], **Matilda Fransson**[2,5], **Theo Suter**[2], **Lukas Helfen**[6], **Cyrille Couture**[6], **Nikolay Kardjilov**[4], **Alessandro Tengattini**[6], **Paul Shearing**[2,3,7] **and Dan Brett**[2]

[1] Department of Materials Science & Engineering, University of Sheffield, Sir Robert Hadfield Building, Mappin Street, Sheffield S1 3JD, United Kingdom
[2] Electrochemical Innovation Lab, Department of Chemical Engineering, University College London, London WC1E 7JE, United Kingdom
[3] The Faraday Institution, Quad One, Becquerel Avenue, Harwell Science and Innovation Campus, The Faraday Institute, Didcot OX11 0RA, United Kingdom
[4] Helmholtz-Zentrum Berlin für Materialien und Energie (HZB), Hahn-Meitner-Platz 1, 14109 Berlin, Germany
[5] ESRF, The European Synchrotron Radiation Facility, CS40220, F-38000 Grenoble, France
[6] Institut Laue-Langevin, 71 Avenue des Martyrs, CS 20156, 38042 Grenoble, Cedex 9, France
[7] Department of Engineering Science, University of Oxford, Parks Road, Oxford, OX1 3PJ, United Kingdom
[*] Author to whom any correspondence should be addressed.

E-mail: j.hack@sheffield.ac.uk

Keywords: polymer electrolyte fuel cell, neutron tomography, water management, flow field design, operando imaging

Supplementary material for this article is available online

OPEN ACCESS

RECEIVED
2 October 2023

REVISED
8 February 2024

ACCEPTED FOR PUBLICATION
2 April 2024

PUBLISHED
12 April 2024

Abstract

Water management plays a key role in ensuring optimum polymer electrolyte fuel cell (PEFC) performance, and flow field design can influence the ability of a cell to balance maintaining hydration, whilst avoiding flooding and cell failure. This work deepens the understanding of water evolution in different PEFC flow channel designs, namely single serpentine (SS), double serpentine (DS) and parallel, using our novel high-speed neutron computed tomography method. We developed our previously-reported method by introducing continuous cell rotation, enabling 18 s per tomogram during 1 h holds at 300, 400 and 500 mA cm^{-2}. The volume of water evolved in the cathode, membrane electrode assembly and anode was quantified, and key mechanisms for water droplet formation in the different flow channel designs were elucidated. The parallel flow field design had the poorest water management, with 47% of the cathode flow channel becoming filled after 1 h at 400 mA cm^{-2}. This significant flooding blocked reactant sites and contributed to unstable cell performance and, ultimately, cell failure at higher current densities. The SS cell displayed the best water management, with only 11% of the cathode channel filled with water after 1 h at 500 mA cm^{-2}, compared with 28% of the DS cathode channel. 3D visualisation and analysis of droplet behaviour elucidated how water 'slugs' in the SS were removed in the gas stream, whereas three of the four parallel cathode flow channels became entirely filled with water plugs, blocking gas flow and exacerbating cell flooding. The new insights gained here are expected to extend to novel flow field designs and image-based models, with the use of *operando* neutron CT demonstrated as a powerful technique for both visualising and quantifying water management in operating PEFCs, as well as deepening the knowledge of droplet behaviour in different flow field types.

1. Introduction

With the urgent need to rapidly decarbonise and move away from fossil-fuel-based technologies, fuel cells, and in particular low-temperature polymer electrolyte fuel cells (PEFCs), have become one of the most promising alternative technologies for applications from transport to stationary power [1].

Since water is produced as the only reactant product, effective water management is essential in PEFCs: too little water within the membrane electrode assembly (MEA) and the cell will not function due to dehydration, too much water and cell flooding occurs blocking reactant pathways and leading to cell failure. Thus, gas is transported through PEFCs *via* so-called 'flow fields', which are patterned channels contained within the bipolar plates that deliver gas to the MEA and remove product water away from it to avoid flooding. Conductive materials like graphite, coated stainless steel, or composites [2] are used to produce the bipolar plates, such that there is good transport of electrons away from the anode and towards the cathode.

There are many design options for flow fields that have been proposed in the literature, with amongst the most common being a 'serpentine' design in which the channel contains a number of bends in a snake-like fashion [3, 4] or a 'parallel' design in which multiple channels (multi-channel) are aligned parallel to each other [5]. Serpentine designs can also contain a single channel (single serpentine (SS)), two channels (double serpentine (DS)) or multi-channel [4]. Some practitioners report that the number of channels influences performance more than the design itself [5], whereas others have indicated that the serpentine-like designs outperform parallel designs [6].

Given the importance of the flow channel on PEFC performance and water management, it is key to understand how species are distributed in the various flow field designs. Previous approaches to understanding water management in PEFCs have included the use of neutron radiography [4, 7–11], observation of flow channels in the cell post-operation [6], the use of fault detection and state-of-health monitoring methods [12, 13], or using modelling approaches [5, 14–16] or electrochemical methods [10, 11, 17] to predict water evolution and flooding. However, few studies have focused on the experimental comparison of water management in different flow field designs [4, 8]. Wu *et al* [4] and Cho *et al* [8] used *operando* neutron radiography to study water distribution in operating PEFCs with serpentine and fractal flow fields, respectively, with Wu *et al* finding that SS flow channels resulted in better performance and water management than double or quad designs. However, due to the through-plane nature of the imaging, it was challenging to understand what (if any) water accumulation occurred on the anode, to what extent channels were filled with water or water formation occurred under flow channel ribs. In-plane radiography has been shown to elucidate the filling of water in the flow channels [7, 9, 18], with Boillat *et al* using in-plane radiography to show that water initially wets the outer-surface of the flow channel [7]. However, information about the type of water droplets present, e.g. slugs, films, plugs or droplets [14] cannot be easily determined through in-plane neutron radiography alone.

Modelling can solve some of the limitations of 2D radiography techniques, by building up a 3D picture of water dynamics inside flow channels [5, 15, 16, 19–21]. Examples include the comparison of straight and wavy channels done by Kaiser *et al* [22], who suggested that wavy channels can improve fuel cell performance and water removal, the work by Liao *et al* [23], who showed that inclusion of a sub-channel can improve water drainage in PEFCs, and the work by Niblett *et al* who developed two-phase models for droplet formation under varying flow conditions in straight channels [24]. A number of modelling studies have proposed the formation of different droplet types (primarily only in straight channels, rather than in entire flow fields), with the suggestion that the gas flow properties can influence the types of droplets formed [24–27]. Some experimental work has been done to support and confirm these models, but these have mostly focussed on either small regions of the flow channel [28], or been radiography studies looking at droplet cross sections [25, 29].

To address the limited experimental understanding of 3D water evolution in different PEFC flow field designs, in this work we apply our recently-reported high-speed neutron CT method [30] to study the water evolution inside three common PEFC flow fields, namely SS, DS and parallel (PAR). Our results show key differences in water evolution and accumulation inside these designs with different channel numbers, and allows for direct correlation between water evolution and cell performance. Finally, through analysis of the water droplets through the entire depth of the flow channel, results highlight key bottlenecks in flow channel designs, e.g. slug formation and channel-blocking. It is expected these results can contribute to the development and validation of future numerical models, as well as deepen the understanding of the important relationship between flow field design and PEFC performance.

2. Experimental and methodology

2.1. Materials and electrochemical methods

MEAs, with areas of 2 cm^2, were prepared by hot pressing two commercial gas diffusion electrodes with loadings of 0.4 mg_{Pt} cm^{-2} (HyPlat, South Africa) onto a GORE Select-M8 membrane (Gore, USA) that had been laser-cut with alignment holes matching those of the compression holes of the cell (figure 1(a)). MEAs were hot pressed at 150 °C for 3 min at 400 psi. The MEA was then assembled into our bespoke fuel cell [30]

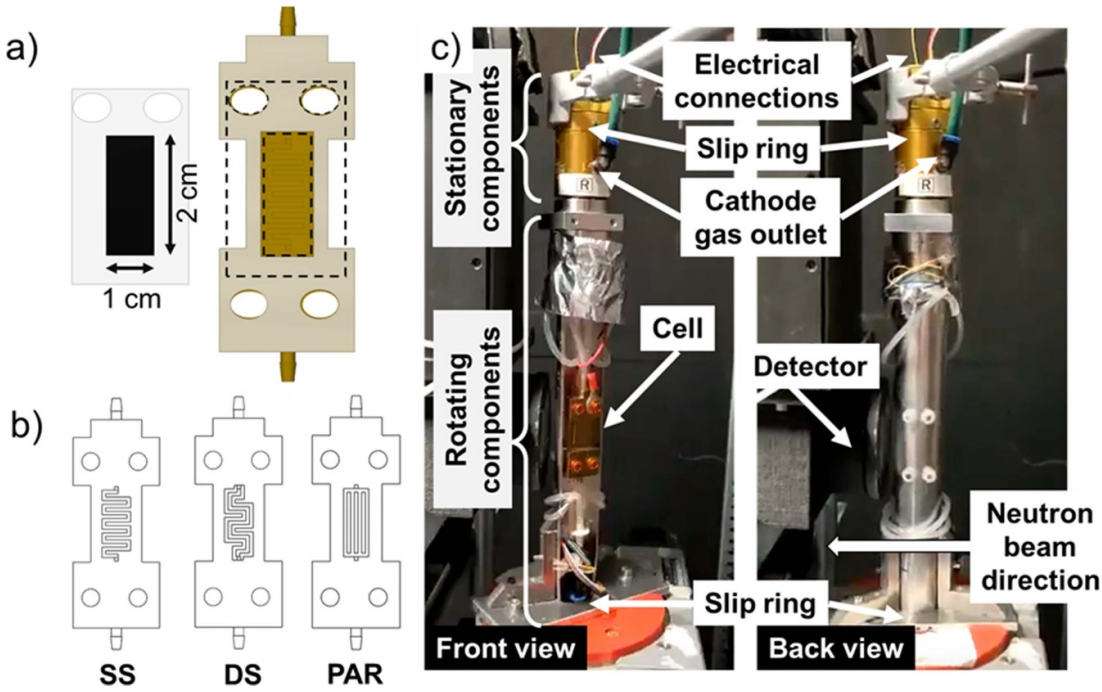

Figure 1. (a) Half-cell view showing the MEA membrane design, dimensions and dashed lines showing the positioning over the gasket and flow field; (b) drawings of the three flow field designs used (SS, DS and PAR). Channel width and depth is 1 mm in all cases; (c) images of a cell assembled on the beamline, with the slip rings indicated on the top and bottom (the bottom slip ring is mounted within the stage out of view), and the rotating components (cell and holder) shown in two views: front and back. The screws can be seen going through the cell to affix it to the holder.

Table 1. Various properties of the three flow channel designs, including the land:MEA contact area, flow channel volume and land:channel ratio.

Flow field design	Land:MEA contact area (mm^2)	Flow channel volume (mm^3)
Single-serpentine	116	84
Double-serpentine	116	84
Parallel	116	84

with the chosen flow field design, and anodised aluminium screws were used to close the cell, providing compression, but ensuring no electrical contact between the two end-plates.

Three different flow field designs were investigated in this work. The SS flow field was reported in our previous study [30], whilst this work focusses on the comparison of three common designs, namely the SS, DS and PAR. The designs, as shown in figure 1(b), have one, two and four channels, respectively. Various properties of the flow fields are shown in table 1, where the land:MEA contact area was calculated using:

$$A_{\text{land:MEA}} = A_{\text{MEA}} - A_{\text{channel}} \tag{1}$$

where $A_{\text{land:MEA}}$ is the area of the land:MEA contact (mm^2), A_{MEA} is the MEA area (mm^2) and A_{channel} is the area of the channel (mm^2). The volume of the flow channel was calculated by multiplying the channel area by the depth of the flow field (1 mm). As shown by the values in the table, despite the significant differences in the flow field geometries, the land:MEA contact area and flow channel volume for each design are the same, 116 mm^2 and 84 mm^3, respectively.

Once assembled, the cells were mounted onto a custom-built holder and attached to the NeXT Beamline at the Institut Laue–Langevin (ILL) [31, 32], with the experimental set-up shown in figure 1(c). Two slip rings (B-COMMAND, Germany) were integrated into the holder and beamline stage, which ensured a continuous gas and electricity connection, allowed for continuous rotation of the cell, and enabled reconstruction of tomograms at any angular turn (e.g. every 180°). To the authors' best knowledge, we have demonstrated the successful use of slip rings for continuous rotation and imaging for operando neutron CT of fuel cells for the first time.

Once mounted, electrochemical measurements and imaging acquisition were carried out at the same time. The purpose of the investigations was to study the evolution of water in the three different flow field designs under 'steady-state' operation. A BioLogic SP-240 potentiostat (BioLogic, France) was used for electrochemical control. Cells were flushed with nitrogen to purge the flow channels fully, before switching to air and hydrogen on the cathode and anode, respectively. Prior to steady-state experiments, three sequential polarisation curves were collected initially without imaging, by sweeping the voltage at 5 mV s^{-1} from OCV to 0.3 V, with recording every 1 s. After collection of polarisation curves, the cells were then purged to eliminate any water accumulated in the flow channels during polarisation, followed by the galvanostatic 'steady-state' holds. Each cell was subject to the same testing procedure matrix, briefly, (A): one-hour galvanostatic holds at 100 mA cm^{-2} intervals increasing from 100 –600 mA cm^{-2} for DS and SS, and 500 mA cm^{-2} for PAR, with 100/20 ml min^{-1} flowrates on the cathode/anode; and (B): one-hour constant-current holds decreasing from 600–100 mA cm^{-2} (for DS) and 500–100 mA cm^{-2} (for SS and PAR), with 100/50 ml min^{-1} flowrates on cathode/anode. Imaging was carried out during all current holds, but stopped in the event that the cell voltage fell below 0.3 V. This work will discuss the results for 500, 400 and 300 mA cm^{-2} at 100/50 ml min^{-1} flowrates, only, since a flowrate of 20 ml min^{-1} on the anode led to excessive cell flooding. This highlights the need for slightly over-stoichiometric flow rates to ensure sufficient reactant supply at high current densities to avoid fuel starvation. Dry gases with no additional humification were supplied in a co-flow arrangement, with gas inlet at the bottom of the cell and outlets at the top, and no additional heating was supplied to the cells. Whilst backpressure was not utilised in this work, future studies could employ backpressure to improve cell performance and demonstrate the effect of backpressure on water management. Between each galvanostatic hold, a nitrogen purge was flowed through the cell to remove any water from the flow channels before the next measurement.

2.2. Imaging and data processing

The experiment was carried out on the NeXT beamline at the ILL, and the set-up was optimised for high-speed imaging, with respect to maximum neutron flux (with a pinhole-sample distance of 5 metres and a pinhole of 30 mm). Given the average sample/detector distance of indicatively 20 mm, we can estimate a neutron blurring (penumbra) of about 120 μm. Imaging was done simultaneously to the electrochemical measurements, and images were collected with 40 Hz, resulting in 1440 projections in 360°, equalling 36 s per tomogram. An infinity corrected detector with an effective pixel size of 16 μm, mounting a 20 μm Gadolinium Oxide scintillator was employed in binning 4, resulting in a final pixel size of ∼64 μm, well compatible with the rest of the setup. Reconstructions were done by using the ASTRA Toolbox [33, 34] in a python script. All projections were dark-field corrected, normalised and outliers, i.e. bright spots from neutrons directly hitting the camera chip, were filtered. Finally, the data sequence was reconstructed with 180° steps between successive neutron CTs. This resulted in 18 s per tomography dataset, which represents half the time of tomograms in our previous work [30] and ensures a balance between temporal resolution and image quality, with exposure times not much greater than some operando neutron radiography studies [4, 35]. This ensures we are capturing water evolution as near to 'real-time' as possible, within the current limits of the technique. After reconstruction, the cathode and anode flow channels and the MEA area were defined and the water volume calculated from the grey values as described in detail in [30]. To calculate the percentage of the channel filled with water, the volume of water was divided by the channel volume (table 1) and multiplied by 100%.

To visualise the spatial distribution of water in the flow channels, tomography datasets were opened in the Avizo image processing software (Thermo Fisher Scientific, US). Segmentation was done using simple thresholding methods, where all voxels above a certain threshold grayscale value were assigned to either cathode or anode 'labels' depending on their spatial location. A 'Dummy' cathode flow channel was also segmented for each flow field type, converted to a surface using the 'Generate Surface' module and visualised using the 'Surface View' module with a 'Transparent' Draw Style, to ensure the water volumes in the cathode and anode could be visualised. After addition of scale-bars and image captions for the corresponding time (in seconds), snapshots were extracted for each time-stamp. Finally, animations were created using the Animation Director, in which each snapshot for a given flow field and current density was imported as an image sequence (0–19 for the twenty snapshots extracted), and the animation created from equal spacing of each snapshot. Animations for each flow field and current density are provided as supplementary information.

Tortuosity factor values and flux concentration maps were generated by importing the segmented flow channel labels into the MATLAB Application TauFactor [36]. The application is a fast and simple tool for calculating the tortuosity factor of the three channel designs, as well as giving a basic indication of regions of relative low and high flux, as discussed further in relation to figure 9.

Finally, to carry out detailed analysis of the droplet behaviour in the various flow channels, which is especially important given the interest in modelling droplet flow [24] and the subsequent need for experimental verification of such models, the 'Label Analysis' module in Avizo (Thermo Fisher Scientific, US) was applied to the segmented cathode label for each current density of the three flow fields. The 'Label analysis' computes the number of individual, unconnected 'particles' (or in this case water droplets) in a 3D image, along with a number of metrics for each particle. For this study, the number of individual 'labels' or droplets is of particular interest to understand more about particle coalescence and evolution in the three different flow field designs. Examples datasets resulting from label analysis can be seen in figure S1, where each discreet droplet has a different colour, and therefore will have its own associated metrics (e.g. BaryCenter, Area or Volume).

3. Results and discussion

3.1. Comparison of electrochemical performance of different flow field designs

Prior to cell imaging, three polarisation curves were collected for each cell and the average performance of these cells is shown in figure 2(a). For data processing, data points in 20 mA cm^{-2} intervals were averaged for the three polarisation curves for each flow field type, and full datasets of all three polarisation curves can be found in the appendix (figure S2). In general, it can be seen that the SS (green diamonds) and DS (orange circles) flow fields result in better performance than the PAR (blue triangles) flow field, with the PAR cell reaching 0.3 V at 580 mA cm^{-2} compared with 680 mA cm^{-2} for both the SS and DS cells. This is also reflected in the power density curves, where the PAR cell had a peak power density of 188 mW cm^{-2} compared with 208 and 205 mW cm^{-2} for SS and DS cells, respectively. The PAR cell did, however, show some improved performance in the transition region between the kinetic and Ohmic regions around 150–200 mA cm^{-2}, as can be seen by the higher potential of the PAR polarisation curve in this region, compared with the SS and DS cells. To investigate the origin of these differences, as well as to gain a deepened understanding of the evolution and movement of water through the various flow field designs, operando neutron CT was performed, as will be discussed in the following sections.

The voltage of each cell during the 1 h galvanostatic holds at 300, 400 and 500 mA cm^{-2} are shown in figures 2(b)–(d), respectively. The PAR cell performance is the poorest, with the cell falling below 0.3 V in both the 400 and 500 mA cm^{-2} tests (figures 2(c) and (d), respectively). During the 400 mA cm^{-2} hold, the PAR cell voltage reaches 0.3 V after 2600 s and during the 500 mA cm^{-2}, the cell voltage reaches 0.3 V after only 240 s. At 500 mA cm^{-2}, the SS and DS performance is similar, with voltages just above 0.4 V, which corresponds well to the polarisation curves in figure 2(a). The performance of the SS cell at 400 mA cm^{-2} and 300 mA cm^{-2} is slightly lower that the DS, which can be explained due to a slightly longer gap between measurements due to unforeseen delays with the neutron beam delivery. From the electrochemistry alone, it is clear that the SS and DS performance over the 1 h steady-state holds are better than the PAR cell, with better cell stability and little drop in cell voltage across the full hour for all current densities. Conversely, the PAR cell voltage drops continuously even during the 300 mA cm^{-2} hold, and falls below 0.3 V after only 240 s during the 500 mA cm^{-2} hold. As will be discussed in sections 3.2 and 3.3, the improved water management of the serpentine-like designs are shown to be a significant contributing factor to the improved performance.

3.2. Evolution of water volume with varying current density

Whilst electrochemical data can give some indication of the effect of flow field design on PEFC performance and water management, the use of high-speed neutron tomography can provide near-real-time quantification and visualisation of water evolution and movement through the flow channels. Furthermore, because of the 3D nature of the technique, it is possible to separate the water residing in cathode, MEA and anode phases, as well as measure water volumes, in comparison with only 2D thickness measurements in neutron radiography. Thus, to provide a deepened understanding the dynamics of water inside the three different flow field designs, the water volumes in each phase (cathode, MEA and anode) were quantified from tomography datasets. Each full tomogram was collected in 36 s, with post-processing resulting in one tomogram per 18 s of operation, as discussed in section 2.2.

Figure 3 shows the evolution of water volume in the three different components of the cells during the one-hour hold at 300 mA cm^{-2} for the different flow field designs, SS (green squares), DS (orange diamonds) and PAR (blue triangles). For all flow field designs, for the MEA (figure 3(b)) the water volume does not rise above around 5–7 mm^3, which indicates that the MEA is in a fully hydrated state. In terms of the cathode (figure 3(a)), it can be seen that the PAR cell has the poorest water management, with steadily increasing water volume up to a maximum of 30.7 mm^3 (37% of the cathode channel filled) at 3600 s. This indicates that water is not being efficiently removed from the flow channels in the gas stream. Furthermore, the current density is relatively low at 300 mA cm^{-2}, which is well within the Ohmic region of the polarisation

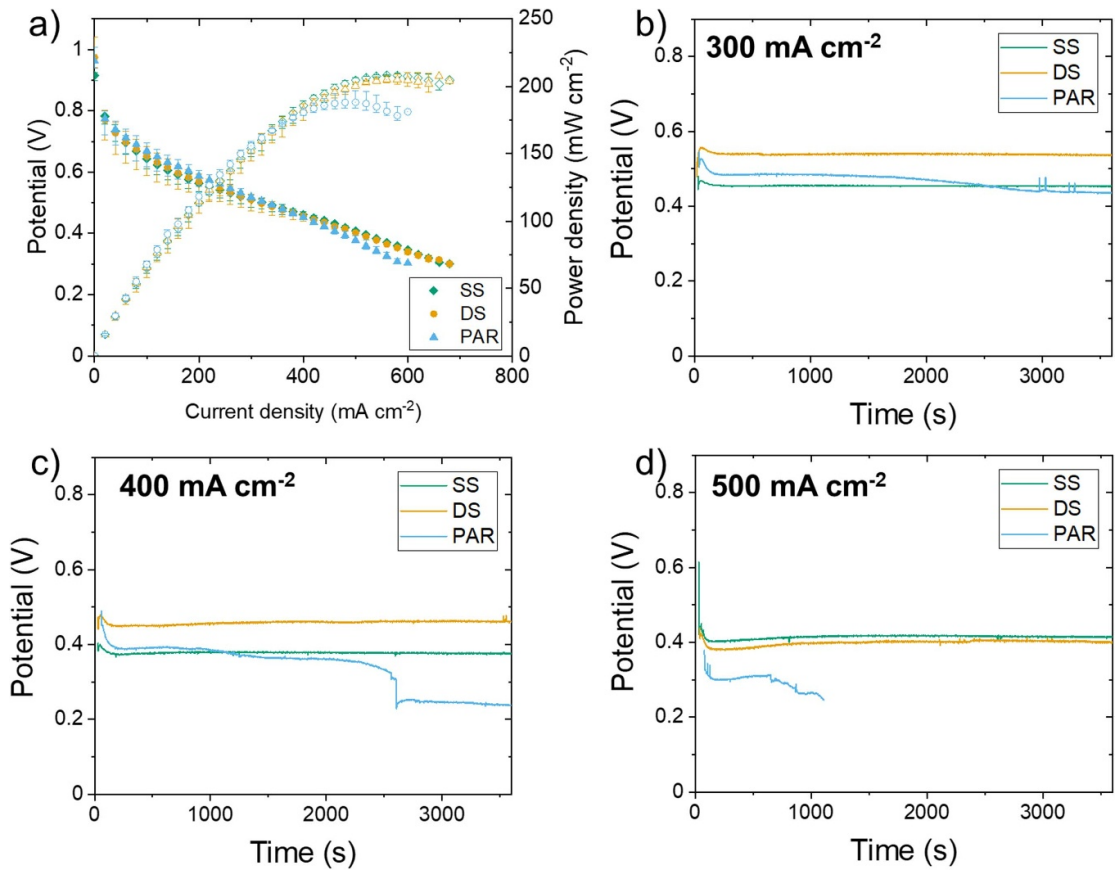

Figure 2. (a) Polarisation curves, (b) SS current holds at 300, 400 and 500, (c) DS current holds at 300–500 mA cm^{-2} and (d) PAR current holds at 300–500 mA cm^{-2}.

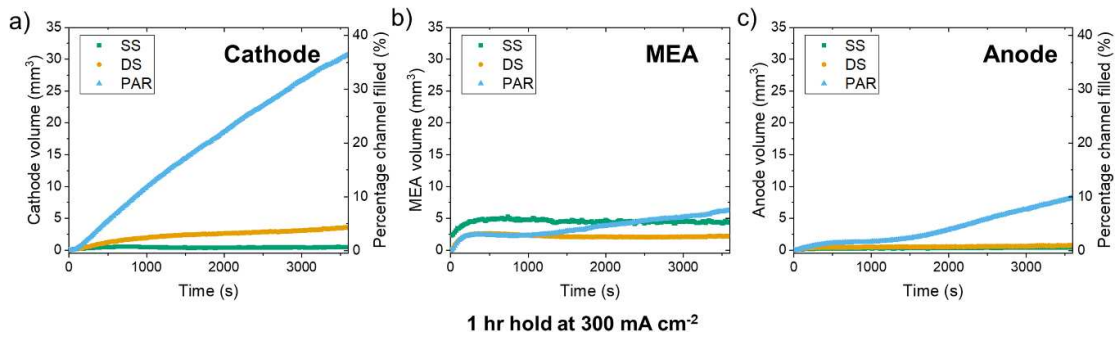

Figure 3. Evolution of water volume in the (a) cathode, (b) MEA and (c) anode of the three different cells at a 300 mA cm^{-2} current hold. The *y*-axis in all graphs shows the corresponding water volume and percentage of the flow channel filled by water, calculated using the values in table 1.

curve (as shown in figure 2). The DS shows a slight increase over the duration of the galvanostatic hold, up to a maximum of 3.6 mm^3 (4% channel filled) at 3600 s, and the SS cell shows the most efficient water removal with only 0.5 mm^3 water in the channel at 3600 s. The poorer water management of the PAR cell is also shown in the anode side (figure 3(c)), where the volume of water in the anode begins to increase from 1500 s to 8.2 mm^3 at 3600 s. The DS and SS cells show no water volume in the anode at 3600 s. This suggests that the accumulation of water on the cathode side has begun to result in water back-diffusion for the PAR cell.

The trends shown during the 300 mA cm^{-2} hold are emphasised further in the results of the 400 mA cm^{-2} hold, as shown in figure 4, with the greatest accumulation of water in the cathode shown for the PAR flow field design (figure 4(a)). The water volume increases at a constant rate until ∼2500 s, where the rate of water evolution slows, to reach a final value of 39 mm^3. This is equivalent to 47% of the channel being filled. This result highlights that flow field and flow channel geometry have a significant impact on water management within the cathode, given that the channel volume for all three flow fields is the same

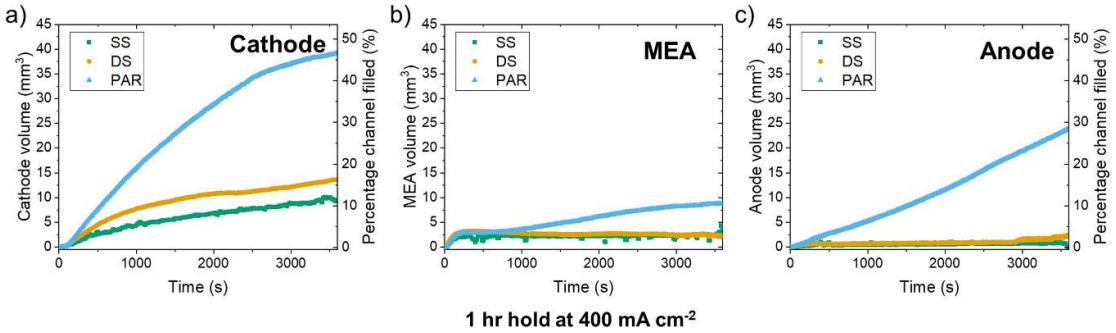

Figure 4. Evolution of water volume in the various flow channels during a galvanostatic hold at 400 mA cm^{-2} in the (a) cathode, (b) MEA and (c) anode. The *y*-axis in all graphs shows the corresponding water volume and percentage of the flow channel filled by water, calculated using the values in table 1.

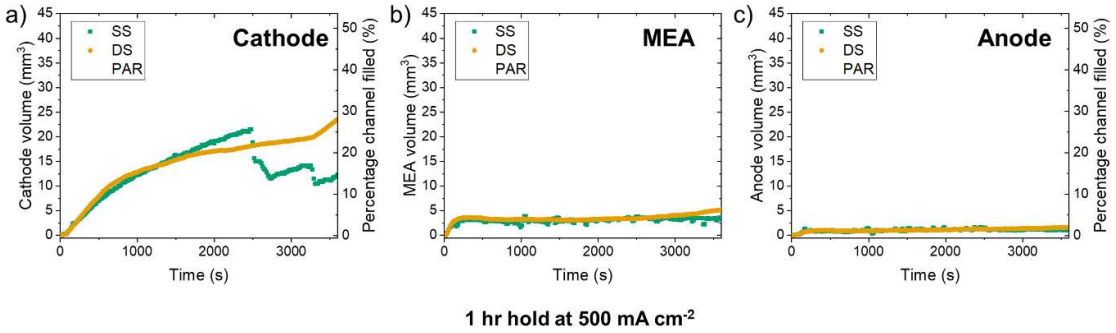

Figure 5. Water evolution in the SS (green) and DS (orange) flow fields for the 500 mA cm^{-2} current hold in the (a) cathode, (b) MEA and (c) anode. The *y*-axis in all graphs shows the corresponding water volume and percentage of the flow channel filled by water, calculated using the values in table 1.

(table 1). The volume of water in the cathode of the DS and SS cells are around four times lower than the PAR cell, with DS cell reaching a maximum water volume of 13.7 mm^3 (16% of channel filled) at 3600 s and SS reaching 9.4 mm^3 (11% filled) at 3600 s. As with the 300 mA cm^{-2} galvanostatic hold, there is also back-diffusion of water to the anode in the PAR cell, only, with a gradual increase in water volume in the PAR anode to 23.8 mm^3. The MEA in the PAR cell reaches a slightly higher value of 8.7 mm^3, which could suggest flooding of the MEA, although resolution of individual MEA components (e.g. the gas diffusion layer (GDL)) is beyond the resolution limit.

The results of water evolution in the DS and SS flow field cells for the 500 mA cm^{-2} galvanostatic hold are shown in figure 5. Since the PAR cell voltage fell below 0.3 V after only 240 s (figure 2(d)), data collection did not proceed and is, hence, not included here. For the cathode (figure 5(a)), the volume in the SS and DS flow channels increase at around the same rate until ∼1650 s (16 mm^3). After this, the water volume in the SS cell increases faster than in the DS cell, until 2480 s. After 2480 s, there is a sharp drop in the water volume in the SS cell, which likely indicates removal of a slug of water (this will be discussed further in section 3.3). The volume then fluctuates between ∼11–15 mm^3 for the remaining time. On the other hand, the water volume in the DS cell continues to increase to a final value of 23 mm^3, corresponding to 28% of the channel being filled. As with the 300 and 400 mA cm^{-2} galvanostatic holds, the MEA water volume and anode water volumes remain low in both flow field geometries, suggesting there is no back-diffusion to the anode. Overall, these results indicate that the SS flow field design is the best in terms of water management, which is in agreement with the findings from 2D radiography studies of Wu *et al* [4].

3.3. Visualisation of water evolution in the flow fields

Imaging datasets for each current density hold for each flow field design were extracted at 180 s intervals for processing in Avizo. The supplementary videos provided show the water evolution through the series of snapshots for each dataset, and these snapshots are also shown at 360 s intervals in figures S3 and S4 for SS@400 mA cm^{-2} and SS@500 mA cm^{-2}, respectively; figures S5–7 for DS@300–500 mA cm^{-2}, respectively; and figures S8 and S9 for PAR@300–400 mA cm^{-2}, respectively. SS@300 mA cm^{-2} is not included, since there was no water accumulated in the SS flow channels during this measurement as a result of the superior water management in this channel design.

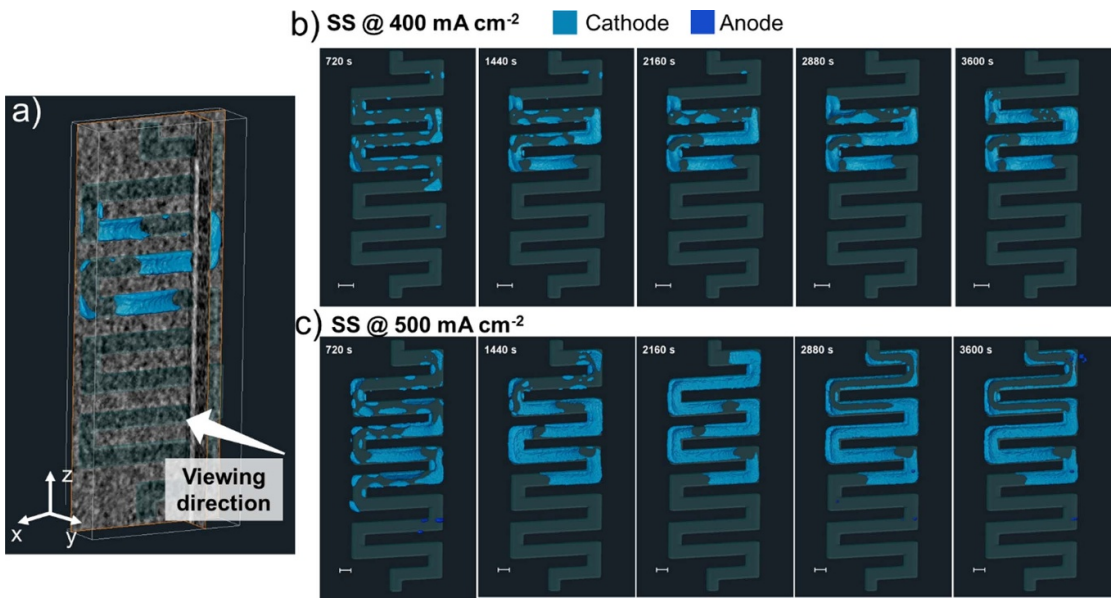

Figure 6. (a) *xz* and *yz* grayscale orthoslices and water volume at 3600 s during the 400 mA cm^{-2} current hold, with the arrow indicating the orientation of all volumes in subsequent images. The viewing orientation is consistent in figures 7 and 8; evolution of water in the SS channel at 540 s intervals starting at 720 s during the (b) 400 mA cm^{-2} and (c) 500 mA cm^{-2} galvanostatic holds. Cathode water is shown in light blue and anode water is indicated in dark blue. The scale bar represents 1 mm in all images.

Figure 6(a) shows the viewing direction and orientation of the volume rendering snapshots in figures 6(b) and (c), as well as figures 7 and 8. It should be noted that the transparent flow field shown for reference is the cathode side, and the MEA is not shown in the figures, but is located between the anode and cathode as can be seen by the light gray/white vertical strip in the *yz* orthoslice in figure 6(a). In general, in both the 400 mA cm^{-2} and 500 mA cm^{-2} current holds (figures 6(b) and (c), respectively), water formation is primarily in the upper half of the SS flow channels on the cathode side, which is in good agreement with the findings from numerical models developed by Padavu *et al* who predicted greater accumulation of water at the flow channel outlet [19]. Given that the cathode gas flow was in an upwards direction through the cell, it is clear that this upwards flow is competing with the effects of gravity (pulling water downwards through the cell), and the known pressure-drop effect [37] resulting in lower gas pressure/velocity at the end of the flow channel and greater water accumulation. As shown in figure 3(a), there was no water formed in the SS anode flow channel during the 300 mA cm^{-2} hold. For both the 400 and 500 mA cm^{-2} holds, there is a very small number of droplets formed in the first 720 s (figures 6(b) and (c), left hand image (720 s)), but these are removed in the anode gas stream by 1440 s.

For the 500 mA cm^{-2} hold, it can be seen that in the top two bends of the SS flow field there is a significant volume of water removed between 2160 and 2880 s (figure 6(c)). This corresponds to the drop in water volume measured, from a maximum of 21.5 cm^3 at 2484 s to 11.5 cm^3 at 2736 s and 10.5 cm^3 at 3312 s (figure 5(a)). The removal of such a 'slug' of water highlights how effective the single channel is at removing the accumulated water in the gas stream, especially considering the gravity effects. Thus, the pressure and flow velocity in the single channel is sufficient to force the removal of such a slug. As will be discussed in relation to the DS and PAR, the single channel holds advantage over the multi-channel designs for ensuring water removal. Another point to note in all cases is the 'convex' film shape of water in all cases, meaning that the water is not entirely filling, and blocking, the channel in any area, but wetting the outer surface of the flow channel. This can be seen most easily in the 2160 s snapshot during the 500 mA cm^{-2} hold (figure 6(c)), where the water in the channel occupies the outer-surface, effectively still leaving a channel for gas to flow through. The result of this is that the cell voltage can be maintained through continuous gas supply to the GDL, as shown in figure 2(d), despite the fluctuation in water volume in the channel. The effect of this wetting on water/gas flow in relation to the droplet types is discussed in further detail, including comparison between the three flow field types, in section 3.4.

The evolution of water in the DS flow field channel is shown in figures 7(a)–(c) for the 300, 400 and 500 mA cm^{-2}, respectively. In contrast to the SS flow channel, the DS has two channels for gas flow, which changes the nature of water formation and accumulation in the channels. For the 300 mA cm^{-2} hold, the water accumulates in only one of the two channels (figure 7(a)), with the majority of water found in the upper half of the cell, as was also observed for the SS cell. In contrast, during the first two-thirds of the

Figure 7. Water evolution in the DS flow fields during the (a) 300 mA cm^{-2}, (b) 400 mA cm^{-2} and (c) 500 mA cm^{-2} galvanostatic holds. Cathode water is shown by light blue and anode water shown in dark blue, although little water in the anode was observed in any of the current holds. The scale bar represents 1 mm in all images.

galvanostatic hold at 400 mA cm^{-2} until around 2160 s, water formation occurs in both channels of the DS design. After 2880 s, all the water has been removed from one of the channels (the left-hand channel shown in figure 7(b)), and the other channel continues to fill until 3600 s. At 3600 s, it can be seen that the channel has been almost completely filled suggesting that gas flow through this channel has been blocked. However, there is little effect of this on the cell performance or voltage profile (figure 2(c), orange line), which suggests that the ease of gas flow through the remaining open channel is sufficient to maintain overall performance. Nonetheless, complete blocking of one channel could affect the degradation/cell performance during extended operation, since regions under the blocked channel would likely be susceptible to gas starvation. The impact of inhomogeneous current distribution has also been described elsewhere by observation of degradation and cracking of the CL [38, 39], and these results further highlight the need to consider reactant and water distribution during operation. A similar water evolution process is observed during the 500 mA cm^{-2} hold (figure 7(c)), where both channels gradually fill with water until 2160 s, after which water is increasingly removed from the right-hand channel, whilst the left-hand channel continuously fills with water and becomes entirely blocked after 2880 s. Unlike in the SS case, there is little evidence for water 'slug' removal during the 3600 s hold, which could be due to the preferential flow of gas through the unimpeded channel. Furthermore, the large water 'slug' in the central bend of the left-hand channel continuously grows and moves downwards through the channel from ~2160 s onwards. This suggests that the gravity effect

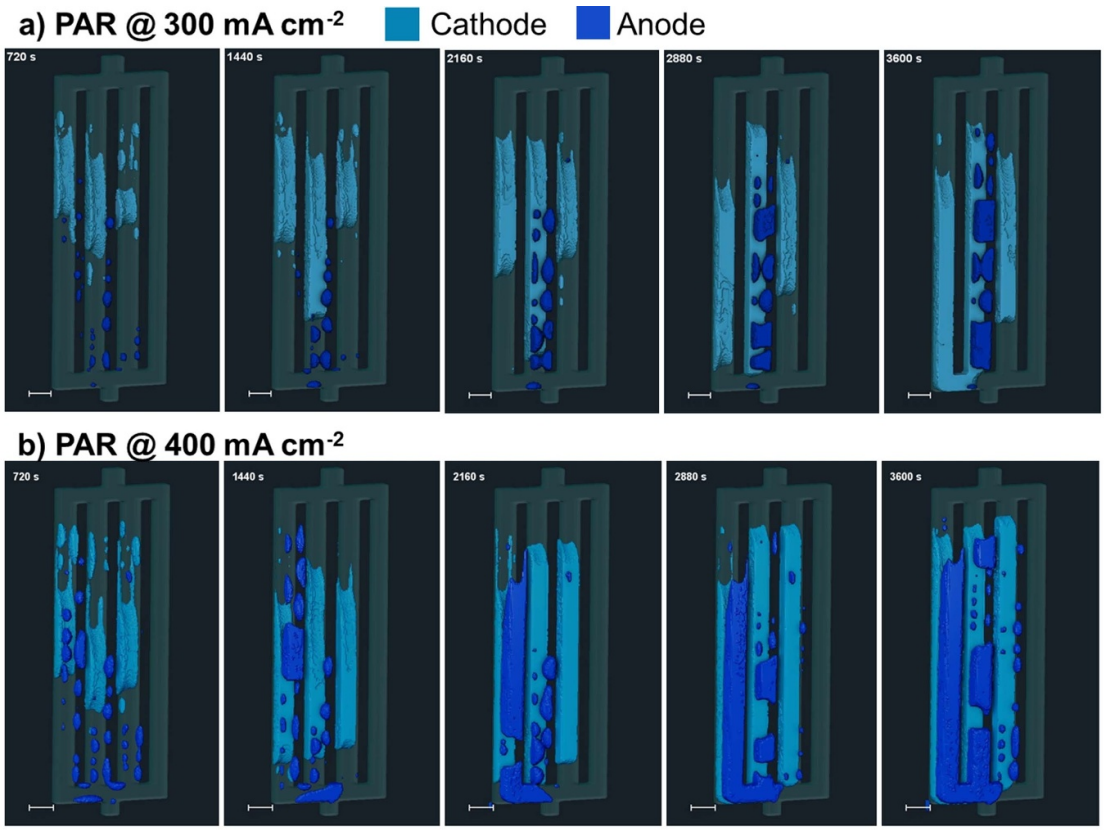

Figure 8. Water evolution in the PAR flow field during the (a) 300 mA cm^{-2} and (b) 400 mA cm^{-2} galvanostatic holds. The cathode water is shown in light blue and the anode water is shown in dark blue. The scale bar represents 1 mm in all images.

pulling this slug of water downwards has overcome the lowered velocity of gas pushing in the opposite direction.

Given that the cell with the PAR channel did not achieve a consistently stable 500 mA cm^{-2}, the water volume evolution in the PAR channels during the 300 and 400 mA cm^{-2} are shown in figures 8(a) and (b), respectively. The differences in geometry of the PAR flow field compared with the SS and DS flow field designs, in particular the lack of channel bends in the PAR design, lead to key differences in water accumulation and management, despite the fact that the land:MEA ratio and channel volume are the same for all three designs, 116 mm^2 and 84 mm^3, respectively (table 1). Unlike the SS and DS designs, even during the 300 mA cm^{-2} galvanostatic hold, there is significant water accumulation across three of the four channels in the PAR flow field (figure 8(a)). Interestingly, despite the symmetry in the PAR design, no water is observed in one of the outer channels (right-hand side of the snapshots in figure 8). During the 300 mA cm^{-2} current hold, the left-middle channel already becomes blocked by 1440 s, with the left-hand channel also blocked by 2160 s. Furthermore, unlike in the case of the SS and DS cells there is a significant volume of water inside the left-middle anode flow channel (dark blue), which indicates that there is back-diffusion occurring from the cathode to anode side as a result of flooding of this channel. The flooding in both the cathode and anode side is further enhanced during the 400 mA cm^{-2} galvanostatic hold (figure 8(b)), where three of the four cathode channels are almost entirely filled with water by 3600 s. The result of this is a continual drop in cell voltage over the first 2600 s, with the voltage dropping just below 0.3 V after 2600 s (figure 2(c)). It is interesting to note than during the initial stages of both the 300 and 400 mA cm^{-2} holds, water accumulation is primarily in the top half of the flow channels. This is consistent with both the SS and DS cases. However, after ~2160 s for the 300 mA cm^{-2} hold and after only ~720 s for the 400 mA cm^{-2} hold, gravity overcomes the reduced velocity in the four channels, resulting in the water in the three channels to begin dropping down towards the cathode inlet. There is, however, enough air velocity at the cathode inlet to avoid complete blocking of the inlet and a clear path remains for gas flow through the unimpeded right-hand channel. It is clear that the limitations of such a straight, multi-channel design, including the lower tortuosity of the channels, and the drop in velocity across the four channels (as a result of the Bernoulli principle), result in very poor water management in the PEFC.

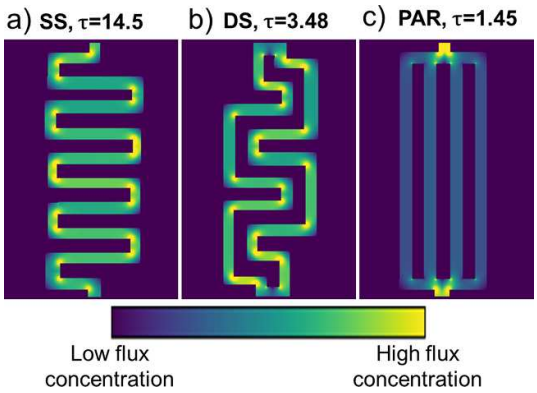

Figure 9. Tortuosity factors calculated for the three flow fields; (a) SS, (b) DS and (c) PAR. Also shown are the simulated flux maps showing areas of relative high (yellow) and low (blue) flux of species in the flow field channels, obtained from the software TauFactor [36]. The relative colour-bar displayed is the same in all cases (set from 0–142).

The poorer water management, in particular for the PAR flow field, can be explained in accordance with the Bernoulli principle and the continuity equation [40], where:

$$\sum A_{\text{in}}\nu_{\text{in}} = \sum A_{\text{out}}\nu_{\text{out}}. \tag{2}$$

With A representing the area of the channel and ν representing the velocity of gas flow. In the case of the PAR flow field, with four flow channels, the area is four times larger (given the four channels are the same width), hence the velocity in each channel will be $\sim$1/4 of the inlet velocity. The lower velocity is also accompanied by a decrease in tortuosity from the SS > DS > PAR (14.5, 3.48 and 1.45, respectively). Looking at the flux concentration maps in figure 9, areas of high flux (yellow) are observed in the inner side of the bends of the serpentine flow fields (SS and DS in figures 9(a) and (b), respectively). This correlates well to the experimental findings for both SS and DS flow channels (figures 6 and 7, respectively), in which water droplets can be seen to be developing in the outer corners of the bends in the earlier stages of the current holds in the areas with lower gas concentration. As discussed previously, the lack of bends and higher number of channels in the parallel design results in lower relative flux across the four channels, which reduces the ability of the cell to remove liquid water in the gas stream and leads to the flooding that was observed in the experimental data. This results in blocking of the flow channels and inhibits reactant gas from reaching active sites, thus reducing cell performance and, ultimately, leading to cell failure.

3.4. Insights into droplet evolution in different flow field type

As mentioned in the introduction, the type of droplet evolved in the flow channel can be directly influenced by the properties of the channel itself. To understand this phenomenon further, and to further investigate how flow channel geometry influences droplet behaviour, a detailed analysis and quantification of droplet formation in the three different flow field types was conducted.

Figure 10 shows the evolution of individual droplets inside the various flow channel types revealing some interesting droplet behaviour for the different flow field designs. Firstly, in general for all three flow fields (SS, DS and PAR for a-c, respectively) the number of droplets inside the channel decreases with increasing time for all current densities, with the exception of DS@300 mA cm^{-2}, which decreases slightly then increases. The overall general decrease indicates that the rate of new droplet formation does not outweigh the coalescence of individual droplets into larger droplets. This effect is most pronounced for the PAR flow field (figure 10(c)), in which the total number of droplets is around 20–25 at the start of the galvanostatic holds, falling to between 3–5 at the end of the galvanostatic holds. Inspecting the visualisations of the PAR water volumes (figure 8), it is clear that 'plug' droplet formation dominates across 3 of the 4 channels, eventually coalescing into one large droplet filling most of these three channels, leaving one open channel for gas to flow through (figure 10(e)).

In the case of the SS, the first 1000 s of both galvanostatic holds are accompanied by a steep reduction and coalescence of droplets, falling from 57 and 68 at 400 and 500 mA cm^{-2}, respectively, at 360 s to 18 and 11 (400 and 500 mA cm^{-2}, respectively) after 3600 s. Furthermore, the number of droplets reaches a minimum at 2340 s for the SS@500 mA cm^{-2} hold followed by an increase until 3600 s, which can be correlated to the removal of a large film of water from the cell (figures 6(c) and S4), making way for further emergence and side-wall droplet formation (figure 10(d)). The wetting of water onto the outer surface of the channel, forms what is thought to be something like a 'microchannel' formed between the water film on the

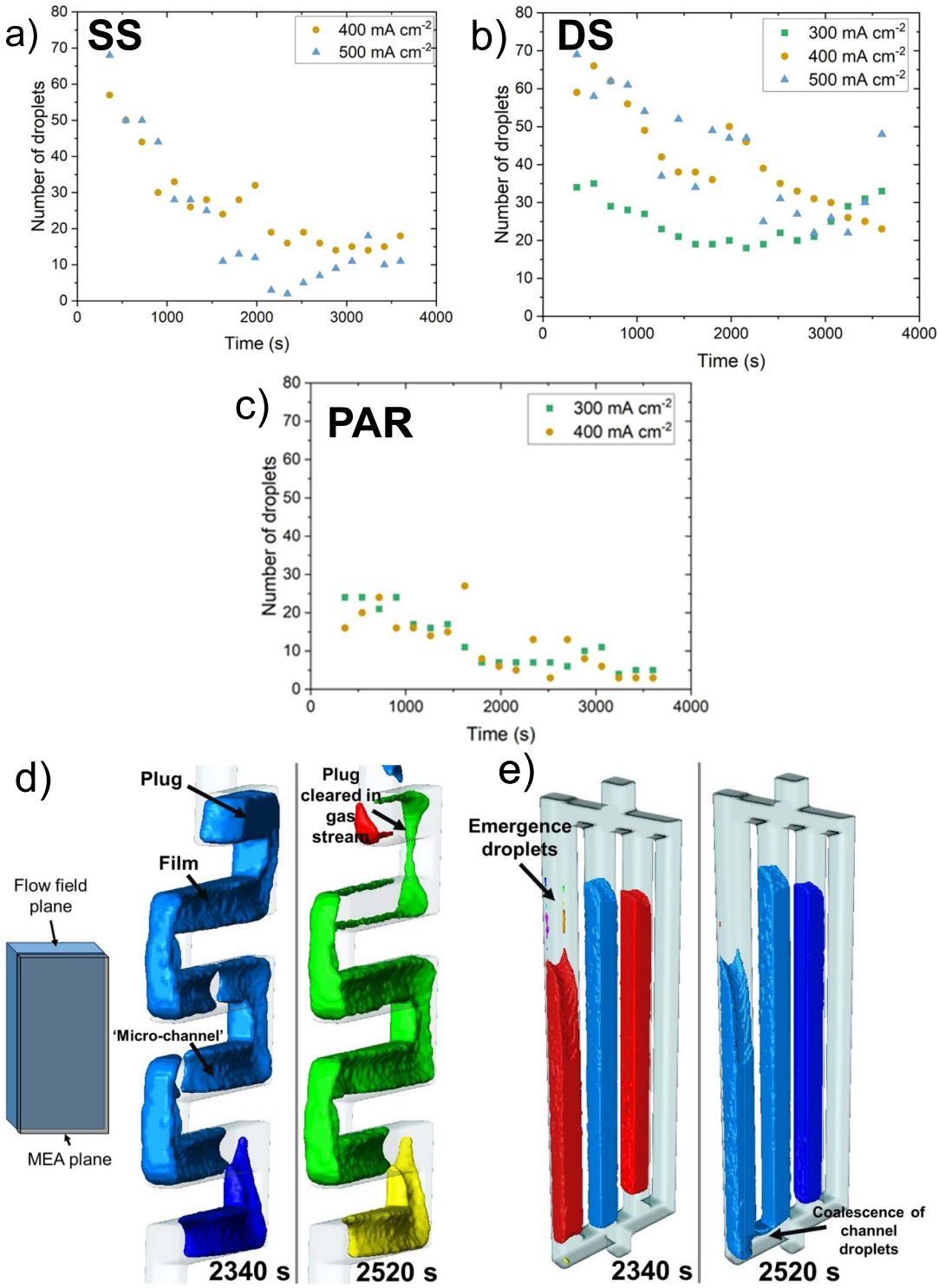

Figure 10. (a)-(c) Graphs showing the evolution of the number of droplets in the cathode flow channel during the holds at various current densities for (a) SS (400 mA cm^{-2}–orange circles; 500 mA cm^{-2}–blue triangles); (b) DS (300 mA cm^{-2}–green squares; 400 mA cm^{-2}–orange circles; 500 mA cm^{-2}–blue triangles); and (c) PAR (300 mA cm^{-2}–green squares; 400 mA cm^{-2}–orange circles). (d) Examples of water droplet types and evolution for the SS@500 mA cm^{-2} hold, where a plug can be seen to be removed from the channel, increasing droplet number (the MEA sits 'on top' of the channel in this case, so the microchannel can be observed (indicated by the inset diagram in (d)); and (e) examples of droplet behaviour in the lower-velocity PAR flow channels at 400 mA cm^{-2}, where emergence droplets can be seen at 2340, which are removed and the two channel plugs coalesce at 2520 s. It should be noted that the 'label' or droplet colours change between datasets, since the Avizo software attributes different label numbers to each droplet in the different datasets. Thus, the colours simply represent discreet droplets and do not have a further meaning here.

outer surface of the channel and the GDL (shown in closer detail in figure 10(d)). The result will be increased velocity in this smaller 'channel', allowing for higher wicking of water droplets away from the GDL surface. Because of the 18 s tomogram^{-1} it could be that the formation and wicking of water on the GDL surface is too fast to be observed here.

The DS cell, with its two channels, seems to be an 'intermediate' case, in which there is a less significant trend in droplet behaviour over the course of each hold. As discussed in section 3.3, the first half of each galvanostatic hold is accompanied by droplet formation in both channels (figures 7 and S5–7). This is overtaken in the second half of the hold by preferential filling of one channel. Thus, one channel is dominated by film and eventually plug formation (especially in the case of the DS@500 mA cm^{-2} hold), while the other channel has some emerging and isolated droplets that are soon cleared in the gas stream.

Overall, clearly the preference for plug formation in the case of the low channel-velocity, multi-channel PAR flow field is a significant contributing factor to the flooding and cell failure of these multi-channel straight designs, when compared with the slugs and films formed in the SS and DS designs. Finally, in the multi-channel designs the clear preference for blocking one/multi-channel, leaving a single gas-flow pathway clearly has implications for novel flow field designs; considering some of the recently reported complex flow field designs, e.g. fractal [41], baffle [42] or foam-type [43], with multiple potential channels for gas flow and distribution, and should be the subject of future studies relating to these designs.

4. Conclusion

Effective water management in PEFCs is essential for ensuring good performance, with a balance between hydration of the membrane for proton conduction and sufficient removal of water to avoid cell flooding. Thus, the choice of flow field design is particularly important for maintaining this balance. Limitations of previous studies comparing flow field designs include those based on theoretical modelling only, or neutron studies employing 2D radiography, where the properties of water can only be understood in terms of thickness.

Using high-speed neutron CT, in which near real-time volume information about water distribution in each PEFC component (cathode, MEA and anode) can be quantified, this work has deepened the insight into the effect of flow field on water evolution in PEFCs. Three different flow field designs, with varying geometries and channel numbers, were investigated, namely SS, DS and parallel (PAR). Polarisation curves gave some indication that the PAR cell performance was the poorest, but analysis of the volume of water accumulated in the cathode and anode PAR flow fields during both a 1 h@300 mA cm^{-2} and 1 h@400 mA cm^{-2} highlighted the superior water management of the serpentine designs. After 1 h at 400 mA cm^{-2}, the PAR cathode flow field was 47% filled with liquid water, compared with 16% and 11% for DS and SS, respectively.

Further image processing and visualisation allowed for qualitative understanding of how the liquid water was distributed in the cells. Whereas water in the PAR cell tended to entirely fill and block multiple flow channels, due to the single channel in the SS design, water was removed as 'slugs, plugs and films' leaving a narrow 'microchannel' for gas flow with water coating the outer surface of the channel. Simple modelling of tortuosity factor and flux concentration maps corroborated the findings of the volume analysis, with the lowered flux in the multi-channel cells playing a role in the less effective water management of the DS and PAR designs. Finally, detailed analysis of the droplets, including droplet number and visualisation of droplet type, revealed that the flow field geometry has a direct impact on the types of droplets formed. While in all cases, there was a general decrease in droplet number with time, resulting from coalescence of droplets, the SS droplet types were mainly isolated slugs and films, whereas the PAR droplet types were primarily emerging and plug types. The DS flow field presented an intermediate case, with one channel filled with plugs and the other channel with mainly isolated droplets. As novel flow field designs are increasingly being investigated, it is expected that high-speed neutron CT will be a powerful method for deepening the understanding of water management in PEFC flow fields.

Data availability statement

The data that support the findings of this study are available upon reasonable request from the authors.

Acknowledgments

J H acknowledges funding from EPSRC (EP/T517793/1), The Faraday Institution (FIRG058) and The Royal Academy of Engineering under the Research Fellowship programme. P R S acknowledges The Royal Academy of Engineering (CiET1718/59). The University Grenoble-Alpes and Institute Laue Langevin are

acknowledged for providing beam time within the proposal allocation https://doi.ill.fr/10.5291/ILL-DATA.UGA-130.

ORCID iDs

Jennifer Hack https://orcid.org/0000-0002-5529-4750
Ralf F Ziesche https://orcid.org/0000-0001-7955-6893

References

[1] E4Tech The fuel cell industry review 2021 2022 (available at: https://fuelcellindustryreview.com/)
[2] Mehta V and Cooper J S 2003 Review and analysis of PEM fuel cell design and manufacturing *J. Power Sources* **114** 32–53
[3] André J, Claude E, Sirac D, Gastaldin D and Rossinot E 2020 PEMFC flow-field design, channel/land width ratio optimization *Fuel Cells* **20** 231–5
[4] Wu Y, Cho J I S, Neville T P, Meyer Q, Ziesche R, Boillat P, Cochet M, Shearing P R and Brett D J L 2018 Effect of serpentine flow-field design on the water management of polymer electrolyte fuel cells: an in-operando neutron radiography study *J. Power Sources* **399** 254–63
[5] Limjeerajarus N and Charoen-amornkitt P 2015 Effect of different flow field designs and number of channels on performance of a small PEFC *Int. J. Hydrog. Energy* **40** 7144–58
[6] Liu H, Li P, Juarez-Robles D, Wang K and Hernandez-Guerrero A 2014 Experimental study and comparison of various designs of gas flow fields to PEM fuel cells and cell stack performance *Front. Energy Res.* **2** 2
[7] Boillat P, Scherer G G, Wokaun A, Frei G and Lehmann E H 2008 Transient observation of 2H labeled species in an operating PEFC using neutron radiography *Electrochem. Commun.* **10** 1311–4
[8] Cho J I S *et al* 2019 Visualization of liquid water in a lung-inspired flow-field based polymer electrolyte membrane fuel cell via neutron radiography *Energy* **170** 14–21
[9] Kulkarni N *et al* 2019 Effect of cell compression on the water dynamics of a polymer electrolyte fuel cell using in-plane and through-plane in-operando neutron radiography *J. Power Sources* **439** 227074
[10] Meyer Q *et al* 2015 The hydro-electro-thermal performance of air-cooled, open-cathode polymer electrolyte fuel cells: combined localised current density, temperature and water mapping *Electrochim. Acta* **180** 307–15
[11] Schneider I A, Dahlen S V, Bayer M H, Boillat P, Hildebrandt M, Lehmann E H, Oberholzer P, Scherer G G and Wokaun A 2010 Local transients of flooding and current in channel and land areas of a polymer electrolyte fuel cell *J. Phys. Chem.* C **114** 11998–2002
[12] Nagulapati V M, Kumar S S, Annadurai V and Lim H 2023 Machine learning based fault detection and state of health estimation of proton exchange membrane fuel cells *Energy AI* **12** 100237
[13] Wang Y, Wu K, Zhao H, Li J, Sheng X, Yin Y, Du Q, Zu B, Han L and Jiao K 2023 Degradation prediction of proton exchange membrane fuel cell stack using semi-empirical and data-driven methods *Energy AI* **11** 100205
[14] Bozorgnezhad A, Shams M, Kanani H, Hasheminasab M and Ahmadi G 2016 Two-phase flow and droplet behavior in microchannels of PEM fuel cell *Int. J. Hydrog. Energy* **41** 19164–81
[15] Chowdhury M Z, Genc O and Toros S 2018 Numerical optimization of channel to land width ratio for PEM fuel cell *Int. J. Hydrog. Energy* **43** 10798–809
[16] Kahraman H and Orhan M F 2017 Flow field bipolar plates in a proton exchange membrane fuel cell: analysis & modeling *Energy Convers. Manage.* **133** 363–84
[17] Choi H, Jang H, Kim J, Kwon O, Yoo H, Cha H, Jeong S, So Y and Park T 2023 Real-time detection of flooding in polymer electrolyte membrane fuel cells using high-frequency electrochemical impedance *J. Power Sources* **580** 233311
[18] Oberholzer P and Boillat P 2014 Local characterization of PEFCs by differential cells: systematic variations of current and asymmetric relative humidity *J. Electrochem. Soc.* **161** F139
[19] Padavu P, Koorata P K and Kattimani S 2023 Model based evaluation of water management and membrane hydration in polymer electrolyte fuel cell with reactant flow-field gradients *Int. J. Heat Mass Transfer* **214** 124460
[20] Kumar A and Reddy R G 2003 Effect of channel dimensions and shape in the flow-field distributor on the performance of polymer electrolyte membrane fuel cells *J. Power Sources* **113** 11–18
[21] Wang N, Qu Z, Zhang G, Tang Z and Wang Y 2023 Cross flow and distribution characteristics in automobile polymer electrolyte membrane fuel cells: a three-dimensional full-scale modeling study *J. Power Sources* **580** 233348
[22] Kaiser R, Ahn C-Y, Kim Y-H and Park J-C 2023 Performance and mass transfer evaluation of PEM fuel cells with straight and wavy parallel flow channels of various wavelengths using CFD simulation *Int. J. Hydrog. Energy* **51** 1326–44
[23] Liao S, Qiu D, Yi P, Peng L and Lai X 2022 Modeling of a novel cathode flow field design with optimized sub-channels to improve drainage for proton exchange membrane fuel cells *Energy* **261** 125235
[24] Niblett D, Holmes S M and Niasar V 2021 Discrete-particle model to optimize operational conditions of proton-exchange membrane fuel-cell gas channels *ACS Appl. Energy Mater.* **4** 10514–33
[25] Cho S C, Wang Y and Chen K S 2012 Droplet dynamics in a polymer electrolyte fuel cell gas flow channel: forces, deformation and detachment. II: comparisons of analytical solution with numerical and experimental results *J. Power Sources* **210** 191–7
[26] Qin C, Hassanizadeh S M, Rensink D and Fell S 2012 One-dimensional phenomenological model for liquid water flooding in cathode gas channel of a polymer electrolyte fuel cell *J. Electrochem. Soc.* **159** B737
[27] Ding Y, Bi X T and Wilkinson D P 2014 Numerical investigation of the impact of two-phase flow maldistribution on PEM fuel cell performance *Int. J. Hydrog. Energy* **39** 469–80
[28] Doerenkamp T, Sabharwal M and Eller J 2021 Insights into the stability and formation of water droplets using operando x-ray tomographic microscopy *ECS Trans.* **104** 75
[29] Hirpara V, Patel V, Zhang Y, Anderson R, Zhu N and Zhang L 2020 Investigating the effect of operating temperature on dynamic behavior of droplets for proton exchange membrane fuel cells *Int. J. Hydrog. Energy* **45** 14145–55
[30] Ziesche R F *et al* 2022 High-speed 4D neutron computed tomography for quantifying water dynamics in polymer electrolyte fuel cells *Nat. Commun.* **13** 1616
[31] Hack J, Fransson M, Helfen L, Kardjilov N, Suter T, Tengattini A and Ziesche R 2021 In operando neutron tomography of polymer electrolyte fuel cell water accumulation (Institut Laue-Langevin (ILL)) (https://doi.org/10.5291/ILL-DATA.UGA-130)

[32] Tengattini A, Lenoir N, Andò E, Giroud B, Atkins D, Beaucour J and Viggiani G 2020 NeXT-grenoble, the neutron and x-ray tomograph in grenoble *Nucl. Instrum. Methods Phys. Res.* A **968** 163939
[33] van Aarle W, Palenstijn W J, Cant J, Janssens E, Bleichrodt F, Dabravolski A, De Beenhouwer J, Joost Batenburg K and Sijbers J 2016 Fast and flexible x-ray tomography using the ASTRA toolbox *Opt. Express* **24** 25129–47
[34] van Aarle W, Palenstijn W J, De Beenhouwer J, Altantzis T, Bals S, Batenburg K J and Sijbers J 2015 The ASTRA Toolbox: a platform for advanced algorithm development in electron tomography *Ultramicroscopy* **157** 35–47
[35] Lee J *et al* 2021 Neutron imaging of operando proton exchange membrane fuel cell with novel membrane *J. Power Sources* **496** 229836
[36] Cooper S J, Bertei A, Shearing P R, Kilner J A and Brandon N P 2016 TauFactor: an open-source application for calculating tortuosity factors from tomographic data *SoftwareX* **5** 203–10
[37] Wang C, Zhang Q, Shen S, Yan X, Zhu F, Cheng X and Zhang J 2017 The respective effect of under-rib convection and pressure drop of flow fields on the performance of PEM fuel cells *Sci. Rep.* **7** 43447
[38] Hack J, Rasha L, Cullen P L, Bailey J J, Neville T P, Shearing P R, Brandon N P and Brett D J L 2020 Use of x-ray computed tomography for understanding localised, along-the-channel degradation of polymer electrolyte fuel cells *Electrochim. Acta* **352** 136464
[39] Garcia-Sanchez D, Morawietz T, da Rocha P G, Hiesgen R, Gazdzicki P and Friedrich K A 2020 Local impact of load cycling on degradation in polymer electrolyte fuel cells *Appl. Energy* **259** 114210
[40] Li Y, Pei P, Wu Z, Xu H, Chen D and Huang S 2017 Novel approach to determine cathode two-phase-flow pressure drop of proton exchange membrane fuel cell and its application on water management *Appl. Energy* **190** 713–24
[41] Bethapudi V S, Hack J, Hinds G, Shearing P R, Brett D J L and Coppens M O 2021 Electro-thermal mapping of polymer electrolyte membrane fuel cells with a fractal flow-field *Energy Convers. Manage.* **250** 114924
[42] Wang X, Qin Y, Wu S, Shangguan X, Zhang J and Yin Y 2020 Numerical and experimental investigation of baffle plate arrangement on proton exchange membrane fuel cell performance *J. Power Sources* **457** 228034
[43] Zhang G, Bao Z, Xie B, Wang Y and Jiao K 2021 Three-dimensional multi-phase simulation of PEM fuel cell considering the full morphology of metal foam flow field *Int. J. Hydrog. Energy* **46** 2978–89